4 Influence of Low Amounts of Oxygen on the Hot Flow Stress of Fire-Refined 99.9% Pure Coppers

4.1 The Residual Composition

The influence of residual elements on the hot flow of 99.9% pure fire-refined coppers remains a field of research. The deleterious effect of Bi, H, Pb, S, Se, Te and Sb has been reported earlier [1,2,3,4,5,6,7]. The use of fire-refined coppers containing detrimental quantities of these elements is now avoided. The phosphorus used during the melt to deoxidize helps prevent embrittlement after soldering. Phosphorus (in contents of ~300 ppm) also reduces the edge cracking effect during hot rolling in the presence of Te [8]. A content of more than 50 ppm of Bi would cause hot rolling problems in the same manner as Te. Contents of Pb appear as globular shape or waxing moon shape inclusions and whose beneficial [5,9,10] or harmful [2,11] effects still need to find a compromise. Some researchers [12,13,14,15] have argued that upon a certain content of oxygen (much higher than in the present work) the Cu_2O particles or inclusions (~4μm) segregate to the grain borders causing voids and cracks during hot working. Coppers with lower oxygen content had been presumed [16] to have oxygen in an interstitial form. The effect of inclusion size particles has been theorized by other researchers [17,18], however failures by void nucleation and coalescence are of no concern for the isolated inclusions found on the fire-refined coppers in this study. When S is kept below ~20 ppm [4] and the residual elements mentioned before are controlled then a fire-refined copper can present desirable hot flow characteristics. The end mechanical properties of a fire-refined copper can be optimized if the influence of the oxygen content and other residual elements is understood.

Early on researchers [3] had reported the strengthening effect of small quantities of oxygen in copper. Later at higher temperatures a reduction on the creep rate as oxygen contents increased was also noticed [19]. More recently Fujiwara [20] and Gao

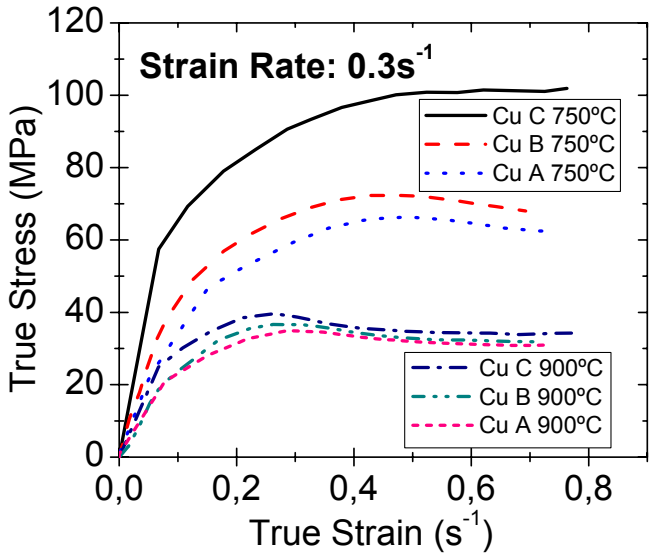

Fig. 4.1. A comparison of the hot flow curves at 750ºC and 900ºC shows that at the lower test temperatures the flow stress differences between the three coppers are considerable.

[21] using high purity coppers indirectly demonstrated that higher oxygen content was responsible for a higher hot flow stress. It was also demonstrated [21] that higher oxygen contents promoted a finer microstructure after dynamic recrystallization. However the latter works attributed the strengthening to solute atom interactions with dislocations. Prediction models commonly deal with this higher than expected strengthening by changing the apparent activation energy without addressing the strengthening mechanism separately. This part of the study addresses the observed hardening [22] when higher oxygen content is present in a fire-refined copper (see fig.4.1). A hardening that cannot be produced by inclusions (whatever their composition) or by interstitial oxygen. Some fire-refined copper users speculated of the presence of other precipitates besides copper oxides, but this study with these coppers reaches a better understanding. Later on another chapter a contribution is made concerning the role of residual elements during dynamic recrystallization conditions.

4.2 Precipitation Hardening during Hot Flow: A Back Stress

Rate equations describing the stress dependence on temperature and strain rate have been proposed [23-26] ever since Garofalo [27] showed that a more general equation was able to describe potential law creep (intermediate to low stress levels) and also exponential law creep (high stress levels). Frost and Ashby [28] proposed

$$\dot{\gamma} = A_2'\left(\frac{D_{eff}\mu b}{kT}\right)\left[\sinh\left(\alpha_2'\frac{\tau}{\mu}\right)\right]^{n'_2}, \tag{4.1}$$

which acknowledges the role of self-diffusion, but also reflects the temperature dependence of the shear modulus. Equation 4.1 expresses the shear strain rate, $\dot{\gamma}$, in terms of shear stress, τ, temperature, T, the effective diffusion, D_{eff}, the shear modulus, μ, the Burgers vector, b, and, the Boltzmann's constant, k. A_2' is a material's constant, which needs to be determined. The exponent n_2' describes the power law and α_2' prescribes the stress level at which the power law breaks down.

Earlier studies on high temperature creep lead to consider that the activation energy for creep in metals was equivalent to the activation energy for self-diffusion, Q_{sd}, which ultimately controlled the deformation process [29]. Recently using a model similar to that employed in creep [30] where stresses due to other obstacles to dislocation movement were treated separately, Cabrera et al. [31-35] have proposed

$$\left[\frac{\dot{\varepsilon}}{D_{sd}(T)}\right]^{1/5} = A\sinh\left\{\alpha\left[\frac{(\sigma-\sigma_0)}{E(T)}\right]\right\}. \tag{4.2}$$

Hereby reducing the discrepancies, which are commonly observed during the determination of constants in eq. 4.1 when the recovery process is affected by another hardening mechanism such as precipitation. Other researchers [16, 21, 26, 36-38] have opted to use an apparent activation energy when other hardening mechanisms become present instead of examining individual strengthening contributions separately.

On eq. 4.2 the self-diffusion coefficient, $D_{sd}(T)$, normalizes the strain rate, $\dot{\varepsilon}$, and a constant exponent of 1/5 is supposed for most metals [23, 39]. Frost and Ashby [28] defined the diffusion coefficient as

$$D(T) = D_{ov} \exp\left(\frac{-Q_{sd}}{RT}\right)$$

where Q_{sd}=197000J/mole is the lattice self-diffusion activation energy and D_{ov} is a pre-exponential constant equal to 2.0 X 10^{-5}m^2/s for copper lattice diffusion. The material constants A and α are determined through a non-linear regression analysis of the strain rate, temperature and stress data. Frost and Ashby [28] also defined the shear modulus as

$$\mu(T) = \mu_o\left(1 + \left(\frac{T-300}{T_m}\right)\left(\frac{T_m d\mu}{\mu_o dT}\right)\right)$$

where T_m = 1356K for copper, the temperature dependence of the modulus is $\left(T_m d\mu/\mu_0 dT\right)$ = -0.54 and, the shear modulus at 300K is μ_0 = 4.21X10^{4}MN/m^2. As is known $\nu = (E-2\mu)/(2\mu)$ where a constant Poisson's ratio of ν = 0.33 can be assumed. The elastic modulus as a function of temperature for copper is then expressed as

$$E(T) = 2.66\mu_o\left(1 + \left(\frac{T-300}{T_m}\right)\left(\frac{T_m d\mu}{\mu_o dT}\right)\right).$$

The term $(\sigma - \sigma_o)$ on eq. 4.2 assures that only the stress contribution belonging to the metal matrix may be the one corrected by the elastic modulus as a function of temperature, $E(T)$. As a consequence the stress required to deform pure copper is

$$\sigma_{Cu} = \sigma - \sigma_o \tag{4.3}$$

where the registered stress σ on a precipitation strengthened material is the sum of the stress corresponding to the matrix (σ_{Cu} in the present case) and a back stress σ_o coming from the extra energy required by dislocations to loop or cut obstacles. When no other strengthening mechanism is present the activation energy for self-diffusion, Q_{sd}, can be used, as the activation energy required for deformation [29]. As has been demonstrated earlier [40] the hot flow behavior of Cu A, which is practically precipitation free, can be easily predicted employing eq. 4.2 and Q_{sd}. Cu A with only 26ppm of oxygen behaves like a large-grained high purity copper thus, the registered stress, σ, of eq. 4.2 is equal to the registered stress for Cu A in the absence of a back stress, $\sigma_{Cu} = \sigma = \sigma_{CuA}$. Equation 4.2 can then be rearranged to express the registered stress, σ, as

$$\sigma = \left(\frac{E(T)}{\alpha}\right)\ln\left[\frac{1}{A}\left(\frac{\dot{\varepsilon}}{D_{sd}(T)}\right)^{1/5} + \sqrt{1 + \left(\frac{1}{A^2}\right)\left[\frac{\dot{\varepsilon}}{D_{sd}(T)}\right]^{2/5}}\right]. \tag{4.4}$$

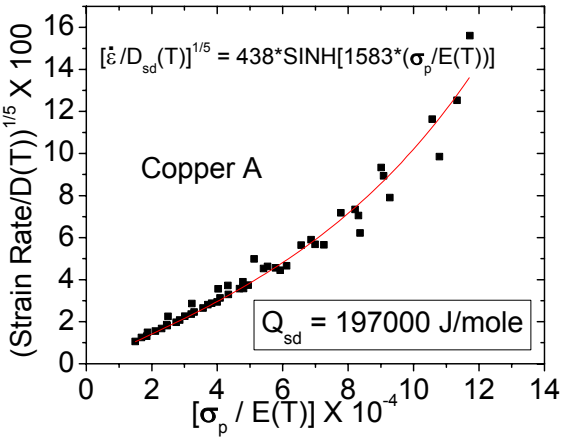

Fig. 4.2. Fit of A_p and α_p using eq. 4.2.

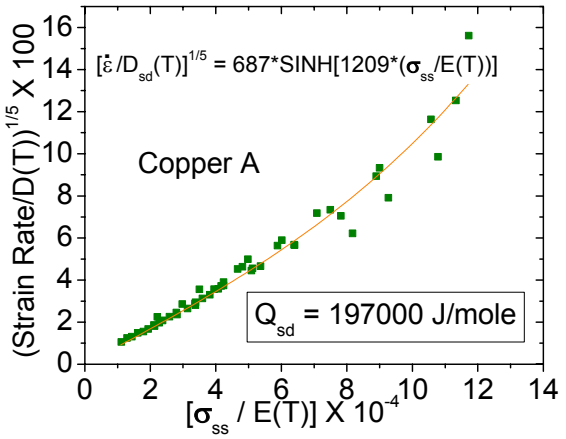

Fig. 4.3. Fit of A_{ss} and α_{ss} using eq. 4.2.

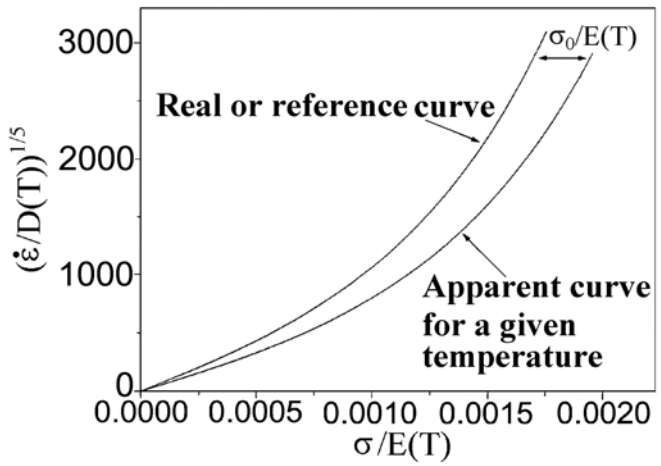

Fig. 4.4. The graph from ref. [41] illustrates eq. 4.2 and the comparative method, which helps determine the back stress, σ_0, for a given temperature, when the real or reference curve of a pure metal is known.

In hot compression tests performed at constant strain rate, any of the characteristic stresses (peak stress, σ_p, or steady state stress σ_{ss}) can be substituted in for the registered stress, σ. Figure 4.2 shows the Levenberg-Marquardt procedure employed while using commercial software (Origin) to determine A_p and α_p, which allow predicting σ_p. The non-linear equation used during the fitting session was y = A sinh(αx) where y and x represented $[\dot{\varepsilon}/D(T)]^{1/5}$ and $\sigma_p/E(T)$ respectively. Figure 4.3 shows the fitting procedure while determining A_{ss} and α_{ss}, which help describing σ_{ss}. The same fitting procedure for Cu B with 46ppm of oxygen and Cu C with 62ppm of oxygen does not produce a reliable correlation. The strengthening caused by the precipitates at lower temperatures (below 850ºC) prevent a normalization of the data points by the self-diffusion coefficient, $D_{sd}(T)$, and by the elastic modulus, $E(T)$. However as fig. 4.4 from ref. [34] shows there exists a comparative method through which the back stress, σ_o, (sometimes called internal stress) can be calculated using the apparent curve at each test temperature.

Table 4.1. Values of A_{CuA} and α_{CuA} at each tested temperature for copper A.

	A_{CuA} for σ_p	α_{CuA} for σ_p	A_{CuA} for σ_{ss}	α_{CuA} for σ_{ss}
600ºC	228	2146	251	2065
650ºC	481	1526	840	1067
700ºC	659	1215	1768	548
750ºC	727	1012	2318	380
800ºC	584	1232	1221	705
850ºC	1267	587	1531	563
900ºC	349	1994	689	1254
950ºC	450	1567	876	973

Table 4.2. Values of A_{CuB} and α_{CuB} at each tested temperature for copper B.

	A_{CuB} for σ_p	α_{CuB} for σ_p	A_{CuB} for σ_{ss}	α_{CuB} for σ_{ss}
600ºC	484	977	737	734
650ºC	416	1124	807	712
700ºC	541	1007	1119	588
750ºC	334	1550	656	1029
800ºC	479	1292	994	762
850ºC	364	1670	849	905
900ºC	657	1014	1194	673
950ºC	270	2361	903	916

Table 4.3. Values of A_{CuC} and α_{CuC} at each tested temperature for copper C.

	A_{CuC} for σ_p	α_{CuC} for σ_p	A_{CuC} for σ_{ss}	α_{CuC} for σ_{ss}
600ºC	139	1669	*	*
650ºC	273	1280	501	893
700ºC	522	844.	1692	317
750ºC	1853	291	3874	159
800ºC	622	895	1256	543
850ºC	415	1378	575	1212
900ºC	428	1500	630	1245
950ºC	672	999	1629	498

* No reliable fit was possible.

If instead of using a general value for A and α as shown for Cu A on figures 4.2 and 4.3, a value for A and α at each temperature can be found using eq. 4.2 and the registered stresses for the three coppers (σ_{CuA}, σ_{CuB} and σ_{CuC}), which would enable to increase the correlation coefficient, R^2, at expense of the normalizing purpose of $D_{sd}(T)$ and $E(T)$. The reference or real curve is the one fitted using Cu A, which is subtracted from the apparent curve, which is due to the strengthening created by the precipitates formed at a particular temperature. Tables 4.1, 4.2 and, 4.3 show the values obtained after fitting for A and α using the peak stress, σ_p, and the steady state stress, σ_{ss}, for each of the three coppers. These values allow a mathematical description of the added back stresses

$$\sigma_{o\ CuB} = \sigma_{CuB} - \sigma_{CuA} \tag{4.5}$$

$$\sigma_{o\,CuB} = \left(\frac{E(T)}{\alpha_{CuB}}\right)\ln\left(\frac{1}{A_{CuB}}\left[\frac{\dot{\varepsilon}}{D_{sd}(T)}\right]^{1/5} + \sqrt{1+\left(\frac{1}{A_{CuB}^2}\right)\left[\frac{\dot{\varepsilon}}{D_{sd}(T)}\right]^{2/5}}\right)$$
$$-\left(\frac{E(T)}{\alpha_{CuA}}\right)\ln\left(\frac{1}{A_{CuA}}\left[\frac{\dot{\varepsilon}}{D_{sd}(T)}\right]^{1/5} + \sqrt{1+\left(\frac{1}{A_{CuA}^2}\right)\left[\frac{\dot{\varepsilon}}{D_{sd}(T)}\right]^{2/5}}\right)$$

and

$$\sigma_{o\,CuC} = \sigma_{CuC} - \sigma_{CuA} \tag{4.6}$$

$$\sigma_{o\,CuC} = \left(\frac{E(T)}{\alpha_{CuC}}\right)\ln\left(\frac{1}{A_{CuC}}\left[\frac{\dot{\varepsilon}}{D_{sd}(T)}\right]^{1/5} + \sqrt{1+\left(\frac{1}{A_{CuC}^2}\right)\left[\frac{\dot{\varepsilon}}{D_{sd}(T)}\right]^{2/5}}\right)$$
$$-\left(\frac{E(T)}{\alpha_{CuA}}\right)\ln\left(\frac{1}{A_{CuA}}\left[\frac{\dot{\varepsilon}}{D_{sd}(T)}\right]^{1/5} + \sqrt{1+\left(\frac{1}{A_{CuA}^2}\right)\left[\frac{\dot{\varepsilon}}{D_{sd}(T)}\right]^{2/5}}\right)$$

due to the precipitation of Cu_2O crystallites. Notice that Equations 4.5 and 4.6 express the added back stress in terms of the strain rate at a constant temperature.

The back stress as an individual strengthening contribution and its dependency on strain rate is shown in figures 4.5 and 4.6 for Cu B and Cu C respectively. The graphs show the functions of the back stresses generated from the steady state stress, $\sigma_{o\,ss}$, and from the peak stress, $\sigma_{o\,p}$, at each tested temperature. The back stresses produced at temperatures above 750ºC are smaller and tend to disappear upon reaching 950ºC. An analysis of the back stress from figures 4.5 and 4.6 allow pointing out several observations. As explained a comparison between coppers B and C show that at the same temperature the back stress is always higher for the copper with higher oxygen content. The back stress is strain rate sensitive like most other stress-related phenomena at higher temperatures. At higher strain rates the back stresses become increasingly higher (although a saturation back stress must exist). The difference between the peak back stress, $\sigma_{o\,p}$, and the steady state back stress, $\sigma_{o\,ss}$, is largest at higher strain rates. In most of the cases here presented, the steady state back stress is higher than the peak back stress at faster strain rates and lower or equal to the peak back stress at slower strain rates. The latter observation can be explained because at higher strain rates the time, $\varepsilon/\dot{\varepsilon}$, is not sufficient for precipitates to fully develop. At slower strain rates the back stress diminishes because the diffusion rate helps dislocations to climb or cross slip with more ease, which allows overcoming obstacles such as the Cu_2O precipitates.

A corroboration, which validates the back stresses calculated with equations 4.5 and 4.6 is that the values obtained for A and α using eq. 4.2 are almost equal to the values reported [40] for copper A, the back stress free copper. Table 4.4 shows the values of A and α of Cu B and Cu C after subtracting the calculated back stress. The

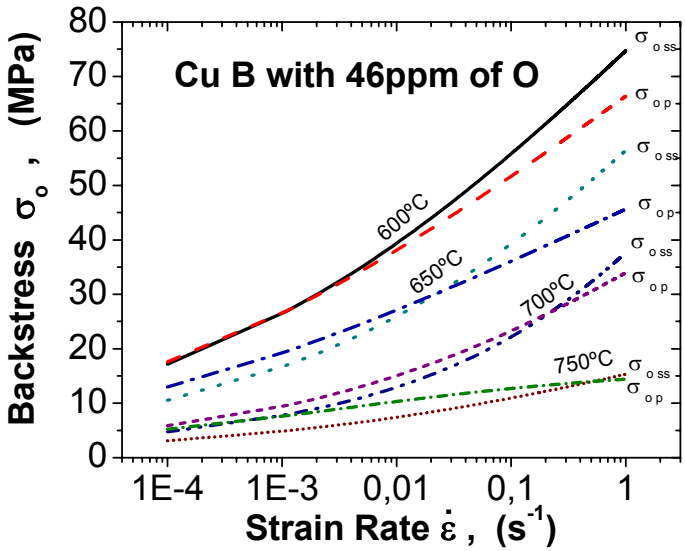

Fig. 4.5. The additional stress or back stress present in Cu B due to precipitation of Cu_2O.

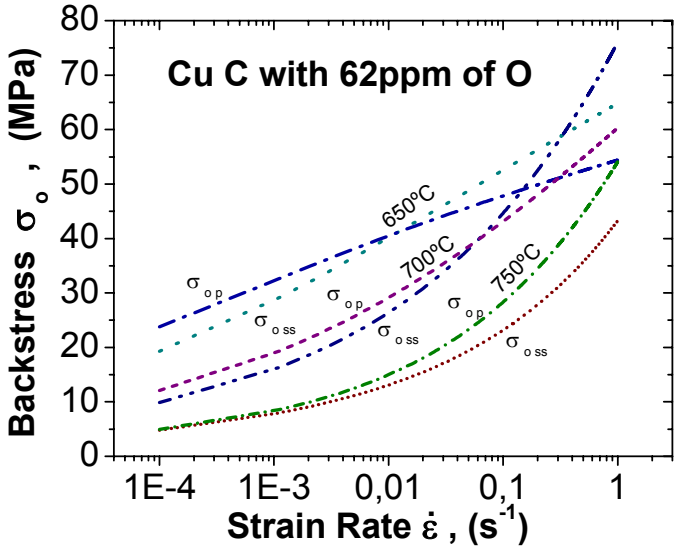

Fig. 4.6. The additional stress or back stress present in Cu C due to precipitation of Cu_2O.

Table 4.4. Values of A and α from eq. 4.2 after subtracting the corresponding back stress described by equations 4.5 and 4.6. Similar values corroborate the procedure.

	A for σ_p	α for σ_p	A for σ_{ss}	α for σ_{ss}
Cu A	438	1583	687	1209
Cu B	437	1584	694	1199
Cu C	437	1585	790	1079

values of A and α belonging to the peak stress equations are similar for the three coppers, as happens for the values of A and α belonging to the steady state stresses. The fitted data for Cu B is shown on figures 4.7 and 4.8 for the peak stress and steady state stress, respectively. Figures 4.9 and 4.10 show the fitted data for Cu C. The small variation

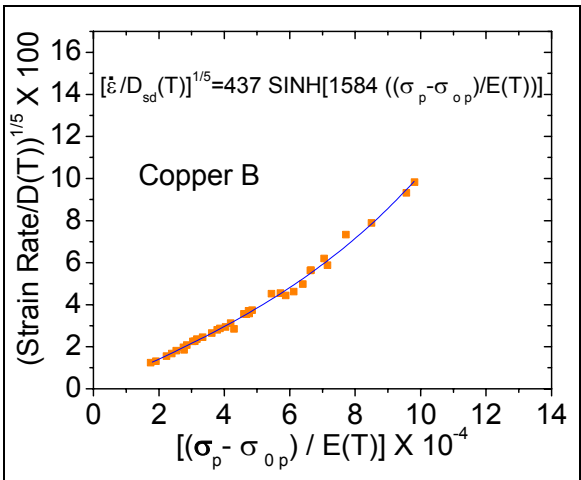

Fig. 4.7. Fit of A_p and α_p using eq. 4.2 after subtracting the back stress from Cu B.

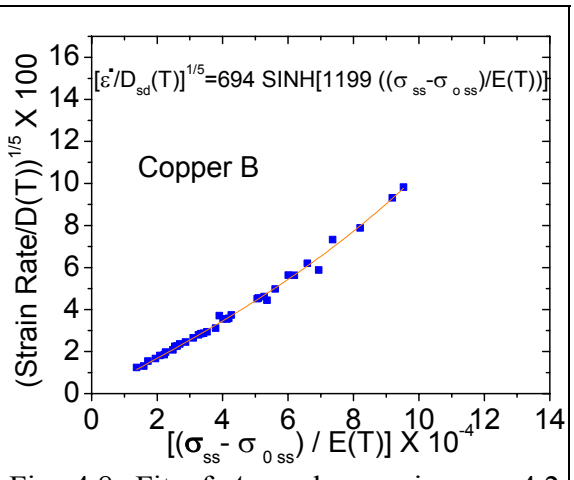

Fig. 4.8. Fit of A_{ss} and α_{ss} using eq. 4.2 after subtracting the back stress from Cu B.

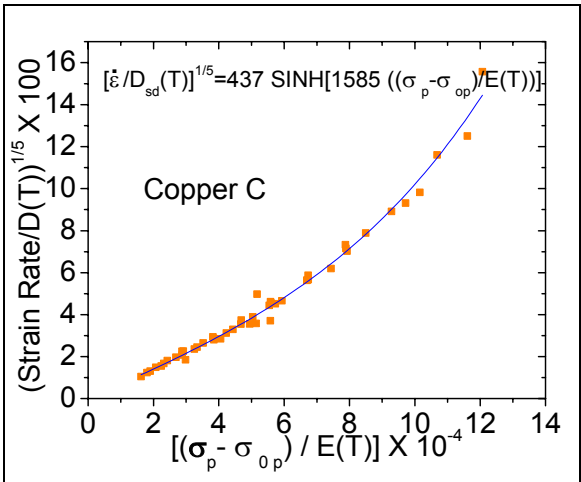

Fig. 4.9. Fit of A_p and α_p using eq. 4.2 after subtracting the back stress from Cu C.

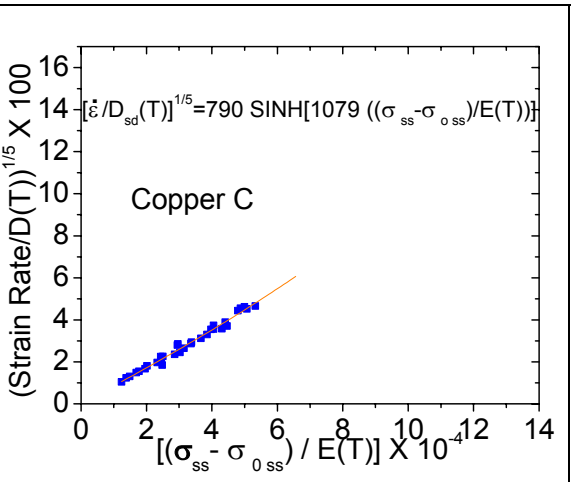

Fig. 4.10. Fit of A_{ss} and α_{ss} using eq. 4.2 after subtracting the back stress from Cu C.

of the parameters in table 4.4 and the normalization of the data points on the $[\dot{\varepsilon}/D(T)]^{1/5}$ versus $(\sigma-\sigma_0)/E(T)$ graphs validate the comparative method for determining the back stress.

From another point of view the back stress, at lower strain rates, tends to zero because dislocation motion is increasingly climb controlled due to the available thermal energy per unit time. However, dislocation motion is glide controlled at higher strain rates and, in the presence of precipitates dislocations are mostly obliged to by pass or cut the obstacles. With the reduction of a dislocation climb mechanism, at a high enough strain rate, the motion of dislocations is limited primarily by the waiting time for dislocations to loop or cut the precipitates. The back stress would saturate at each temperature and become strain rate insensitive. The strength of the precipitates, which is dependent on the size and volume fraction at each temperature, would determine the saturation magnitude of the back stress. On the other hand the stress registered during a compression test remains strain rate sensitive, even at much higher strain rates [36]. When precipitation hardening occurs at room temperature, dislocation glide is the only deformation mechanism present (diffusion enhanced dislocation climb is relatively less important) thus a saturation point is reached and the added reinforcement due to

precipitates is almost constant at any strain rate. Figures 4.5 and 4.6 show a portion of strain rates where the thermal component of the back stress becomes predominant. The other component of the back stress, which is athermal, can be evaluated supposing a point of saturation at each given temperature and strain rate and then using precipitation-hardening theories.

4.3 Precipitation of Cu_2O in Copper

The compression tests of coppers A, B and, C showed a considerable hardening at 600ºC to 750ºC as the oxygen content increased (see fig. 4.1). Precipitation hardening appeared to be the explanation. The finding of Cu_2O crystallites finally cleared the question of which precipitate could be forming on these fire-refined coppers that also contained several ppm of residual elements. Hence the Cu-O phase diagram [41] shown on fig. 4.11 can be used to quantify the volume fraction of Cu_2O particles, however some assumptions need to be made. The concerned part of the Cu-O diagram should be marginally affected by the other residual elements and by the stresses registered. The precipitation volume fraction as a function of temperature can thus be obtained as shown on fig. 4.12, using [42] a mean density of 6.0g/cm^3 for Cu_2O and 8.96g/cm^3 for Cu. The volume

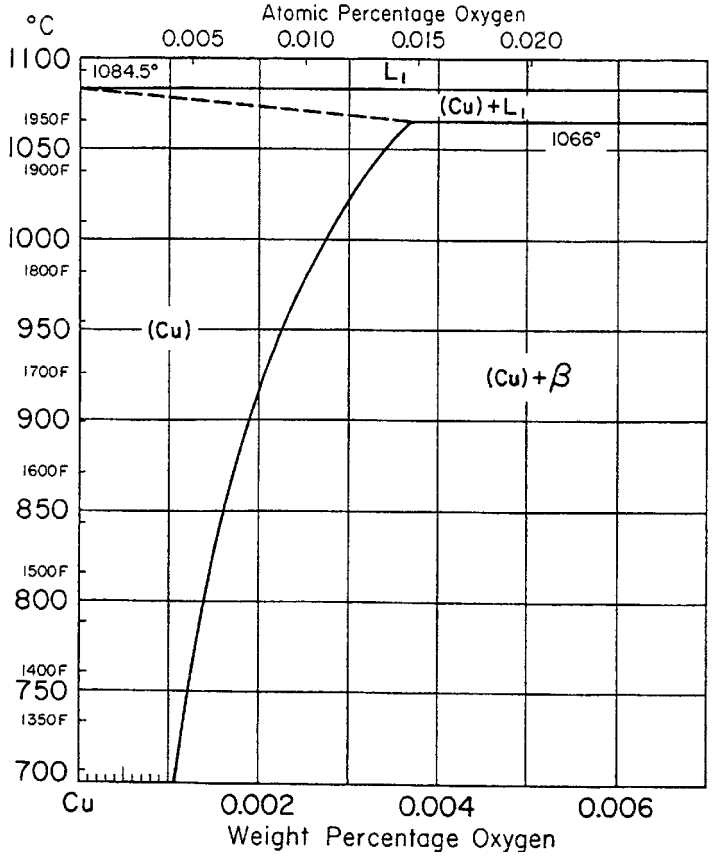

Fig. 4.11. Part of the Cu-O phase diagram corresponding to low amounts of oxygen from ref. [31]. The phase β is Cu_2O, which reduces in volume fraction as temperature increases and reaches 1066ºC. However the presence of impurities may alter the formation of Cu_2O.

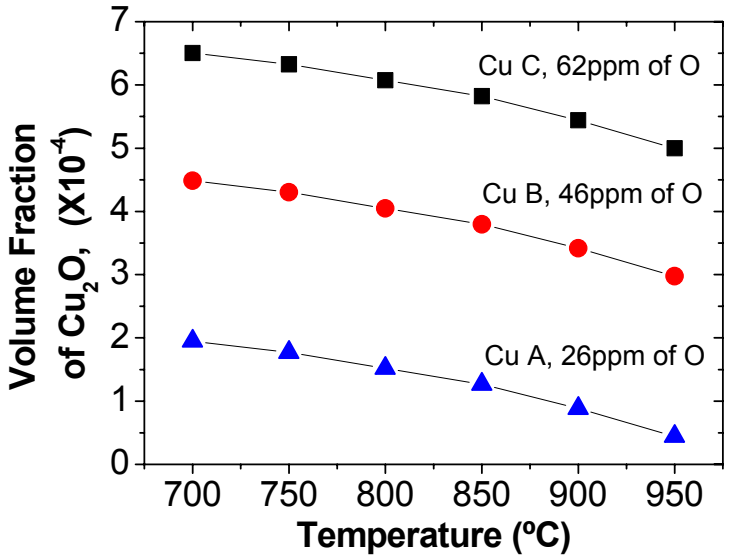

Fig. 4.12. Calculated volume fraction of Cu_2O in the three coppers versus temperature.

fraction reduction as the temperature increases reflects the behavior of the Cu-O phase diagram when the mass percentage of oxygen is close to 0.0037. The maximum solubility of oxygen in solid copper is 0.0037% in mass at 1066ºC and decreases with temperature. The excess oxygen forms Cu_2O. The approximate volume fractions of Cu_2O at 750ºC, given the assumptions exposed above, are 1.77203 X 10^{-4}, 4.30322 X 10^{-4} and, 6.32774 X 10^{-4} for Cu A, Cu B and Cu C respectively.

4.4 Models for Discrete-Obstacle Controlled Plasticity

Physically based rate equations have been developed, which take into account the strain rate produced when a density of mobile dislocations has an average velocity controlled by the waiting time at obstacles [43]. However difficulties in quantifying the dislocations' average velocity lead to the creation of an expression containing the total free energy, ΔF, required to cut or by-pass obstacles without the aid from external work [44]. Frost and Ashby [28] reported on the progress of Evans and Rawlings [45], Kocks et al. [44], De Meester [46] and presented

$$\dot{\gamma} = \dot{\gamma}_0 \exp\left\{-\frac{\Delta F}{kT}\left[1-\left(\frac{\tau}{\tau_{0K}}\right)^p\right]^q\right\} \tag{4.7}$$

where

$$\dot{\gamma}_0 = \frac{\alpha}{b}\left(\frac{\tau}{\mu}\right)^2 \beta b \upsilon \approx 10^6 s^{-1}.$$

On eq. 4.7 $\dot{\gamma}$ describes the shear strain rate in terms of temperature, T, and the resolved shear stress, τ. The pre-exponential, $\dot{\gamma}_0$, can be considered as constant when ΔF is

large (as here). The mechanical threshold stress, τ_{0K}, is the flow strength of a solid at 0 K. Equation 4.7 is also known as the Mechanical Threshold Stress (MTS) Model [47]. When ΔF is large then the influence of exponents p and q is minimum [28], and for discrete obstacles $p = q = 1$. Table 4.5 shows the approximate values of ΔF and τ_{0K} in the presence of various obstacles. A surprising fact is that τ_{0K} is proximate to the theoretical yield stress increment, $\Delta\tau_{ys}$, predicted by Orowan [48] for strong (incoherent) precipitates, $\mu b/\ell$. However, Gladman [49] has shown that Orowan's original relationship overestimates the observed added strengthening. Moreover Frost and Ashby [28] mention two other problems encountered when applying eq. 4.7. The Peierls-Nabarro force or lattice resistance masks the influence of eq. 4.7. Also when using data obtained from polycrystals the appropriate Taylor factor should be $M_s = 1.77$ for f.c.c. metals according to Kocks [50] and not the familiar value of M = 3.07 given by Taylor [51], Groves and Kelly[52]. Other researchers [53] have used the MTS model to study high purity OFHC copper during hot flow, however the predictions miss the experimental results by an amount similar to the stress differences in the coppers investigated on this study. Equation 4.7 was not used during the present work because of the poor correlation obtained when fitting for ΔF and τ_{0K}, and the uncertainty raised when converting from a mono crystalline relationship to a polycrystalline relationship. Instead the added strengthening observed during hot working was analyzed using precipitation hardening relationships (adapted for higher temperatures) and supposing a saturation back stress at higher strain rates. As with relationship 4.7 the precipitation hardening relationships also require knowing whether the precipitate (Cu_2O) is incoherent (strong) or semicoherent (soft) and then depending on the particle size and volume fraction the increase in stress can be predicted.

Table 4.5 Characteristics of obstacles as defined by Frost and Ashby [28] for eq. 4.7.

Obstacle Strength	ΔF	τ_{0K}	Example
Strong	$2\ \mu b^3$	$> \mu b/\ell$	Dispersions; large or Strong precipitates (spacing ℓ)
Medium	$0.2\text{-}1.0\ \mu b^3$	$\approx \mu b/\ell$	Forest dislocations, radiation damage; small or weak precipitates (spacing ℓ)
Weak	$< 0.2\ \mu b^3$	$\ll \mu b/\ell$	Lattice resistance; Solution hardening (solute spacing ℓ)

4.5 Modeling Precipitation Hardening at Higher Temperatures

The interface of a precipitate can form a coherent, semicoherent and/or incoherent union with the metal matrix. When calculating the stress increase due to precipitates then the nature of the precipitate interface acquires an essential relevance, because the nature of the union determines the type of analysis to follow. If the precipitates can be considered semicoherent then the mechanism that explains the added strengthening involves the waiting time for dislocations to cut the crystal lattice of the second phase. On the other hand if the precipitates are incoherent then the added strengthening is produced by the waiting time for dislocations to loop and in this way by pass the obstacles. A higher stress is required for deformation in any of the two cases. The added strengthening of a semicoherent precipitate will depend not only on the "strongness" of the phase but also on the volume fraction present *f*, the average precipitate size and the constrained misfit strain, ε_m. Precipitates that form a semicoherent union distort the metal matrix around them creating a stress field, which produces a greater strengthening effect [49] than would be expected from analyzing the precipitates alone (at any stage of formation or in any type of agglomeration). The added strengthening due to an incoherent precipitate can be predicted knowing the volume fraction and the particles' size. The theoretical coherency between the Cu_2O particles and the Cu matrix at room temperature can be calculated [54].

The coherency between planes of Cu_2O and Cu will depend on the interplanar spacings of the matching crystal planes and on the dilation of the lattice parameters with a higher temperature. If unstressed interplanar spacings are first supposed then the disregistry or misfit between two lattices (δ) is defined by

$$\delta = \frac{d_{Cu_2O} - d_{Cu}}{d_{Cu}} \tag{4.8}$$

where d_{Cu_2O} is the interplanar spacing of the matching Cu_2O side and d_{Cu} is the spacing of the Cu side. When $\delta > 0.25$ then more than one dislocation for every four interplanar spacings would be needed to accommodate the union, but the dislocation cores would then overlap and the interface cannot be considered as coherent [54], i.e. the precipitate face is incoherent. Many of the interplanar combinations between Cu_2O and Cu give a misfit between lattices lower than 0.25, thus at room temperature Cu_2O precipitates can be considered semicoherent. The semicoherency of the newly formed precipitate distorts the metal matrix and a new local lattice parameter a'_{Cu} appears. The *in situ* or constrained misfit ε_m is defined by

$$\varepsilon_m = \frac{a_{Cu_2O} - a'_{Cu}}{a'_{Cu}} \tag{4.9}$$

where a_{Cu_2O} is 0.42696nm. Unfortunately the mean value of ε_m cannot be calculated easily. At room temperature ε_m usually [54] lies in the range $0.5\delta < \varepsilon_m < \delta$. However the use of such misfit strain values at higher temperatures predicts an unreasonably high strengthening. The difficulty in calculating the misfit strain at the temperatures used to compress the copper cylinders was overcome by an iterative approach, where several misfit strains were supposed, each trial produced a stress increase curve, which in the

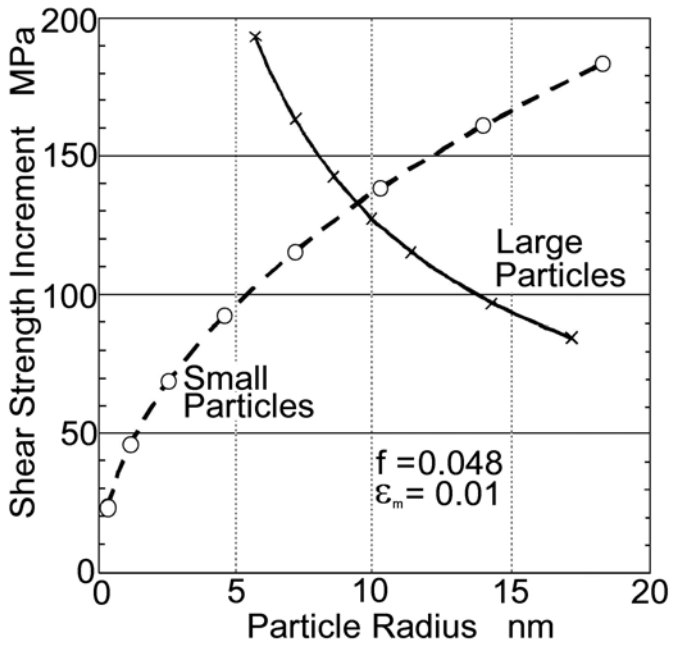

Fig. 4.13. Plot from ref. [49] illustrates the effect of increasing the particle size while using the "small particle" and "large particle" coherency strengthening equations 4.10 and 4.12. A maximum strengthening will be attained at the critical particle size, r_c, and the magnitude of this maximum will be dependent upon the magnitude of the fractional coherency strain, ε_m, and the volume fraction of particles, f. The intersection of both curves marks the critical particle size.

case of a given volume fraction of Cu_2O the stress increase curve only depended on the precipitate radius.

Gladman [49] arrived to a more plausible relationship between the critical precipitate radius, r_c, at which a maximum strengthening is reached and the misfit strain, ε_m, by bounding the validity of strength increment equations applied to precipitates considered small and precipitates considered large. One solution [49] for small semicoherent precipitates after applying a Taylor factor of 3.07 to convert from shear stress to compressive stress is

$$\Delta\sigma_{y(Small)} = 12.587\mu\varepsilon_m^{3/2}(rf/b)^{1/2}. \quad (4.10)$$

Equation 4.10 expresses the yield stress increase (MPa) in the presence of small particles, $\Delta\sigma_{y(Small)}$, in terms of the shear modulus μ, which is dependant on temperature. The semicoherent precipitate radius is r, the volume fraction of precipitates is represented by f, and the Burgers vector is b. A solution [49] for large semicoherent precipitates after applying the appropriate Taylor factor is

$$\Delta\sigma_{y(Large)} = 2.149\mu f^{1/2}\varepsilon_m^{1/4}(b/r)^{3/4}. \quad (4.11)$$

Equation 4.11 only expresses the yield stress increase in the presence of "large" particles. However by making equal the solutions for small (eq. 4.10) and large (eq. 4.11) semicoherent precipitates then one may arrive to

$$r_c = \frac{1}{4} b \varepsilon_m^{-1} \tag{4.12}$$

where the critical precipitate radius, r_c, denotes the intersection of equations 4.10 and 4.11. Relationship 4.12 shows that the misfit strain is dependent on the particle size regardless of the volume fraction. The plot on fig. 4.13 from ref. [49] shows that when equations 4.10 and 4.11 intercept on a $\Delta\sigma_y$ versus r plot then the maximum predicted strengthening occurs for a given particle size and its corresponding misfit strain. Equation 4.10 increases with increasing radius size, but eq. 4.11 decreases with increasing radius size. When eq. 4.10 intercepts eq. 4.11 the rest of eq. 4.10 is considered to lose significance and the equation that from then on predicts the increase in yield strength is eq. 4.11.

The following analysis will demonstrate that at temperatures where an added back stress was found, the coherency seems to obey incoherent precipitation hardening relationships rather than the explained semicoherent hardening relationships. Figures 4.5 and 4.6 show the added back stress of two characteristic points of the hot flow curve (the peak and the steady state). Figures 4.5 and 4.6 also show that the difference between these characteristic points is not great at the strain rate of concern ($0.3s^{-1}$), which can lead to believe that the increase in yield stress is of the same stress increase happening on the rest of the points of the hot flow curve thus $\Delta\sigma_y \approx \sigma_0$ at $0.3s^{-1}$. The assumption that an increase of peak or steady stress can be compared to an increase of yield stress is necessary, because measuring the yield stress from hot flow curves in copper is neither precise nor accurate. The use of 750ºC and $0.3s^{-1}$ curves and TEM samples minimizes the presence of the back stress thermal component, which allows dislocations to climb and dynamically recover from the additional hardening. Figure 4.14 shows the yield stress increment predicted for Cu A by equations 4.10 and 4.11 when using the misfit strain calculated using relationship 4.12. The arrows point to the interception of the two equations and also name the particle radius used to calculate the misfit strain in relationship 4.12. The smallest particle found in Cu A had a radius of 16.5nm and the predicted maximum yield stress increment is of 9.7MPa. However the possibility of being able to use the self diffusion activation energy to correlate stress, strain rate and temperature demonstrated that Cu A behaves like a back stress free copper. The rest of the arrows are only indicative of a possible behavior, because no smaller particles were found during the TEM analysis.

Figure 4.15 shows the predicted yield stress increment in Cu B due to the largest particle found (3.459nm) on the TEM samples. One cannot assure a largest particle radius present because TEM samples only survey a small volume of material. The smallest Cu_2O particle found in Cu B had 2.5nm. The strengthening predicted for the smaller radius found (2.5nm) on Cu B is not signaled with an arrow, because the prediction is thought to be too high and unlikely. For comparison purposes the maximum strengthening predicted for the radii found (5.00nm and 7.188nm) on Cu C were also calculated for Cu B and are also shown on fig. 4.15. Equations 4.10 and 4.11 overestimate the strengthening observed at 750ºC on sample Cu B even for the largest particle shown. Despite that the largest particle (7.1875nm) was found on Cu C such particle size in Cu B should produce a stress increase of 34.8MPa according to fig. 4.15. However the peak back stress observed is only of 13.6MPa and 13.0MPa for the steady state back stress. The Cu_2O particles in Cu B do not seem to behave semicoherently.

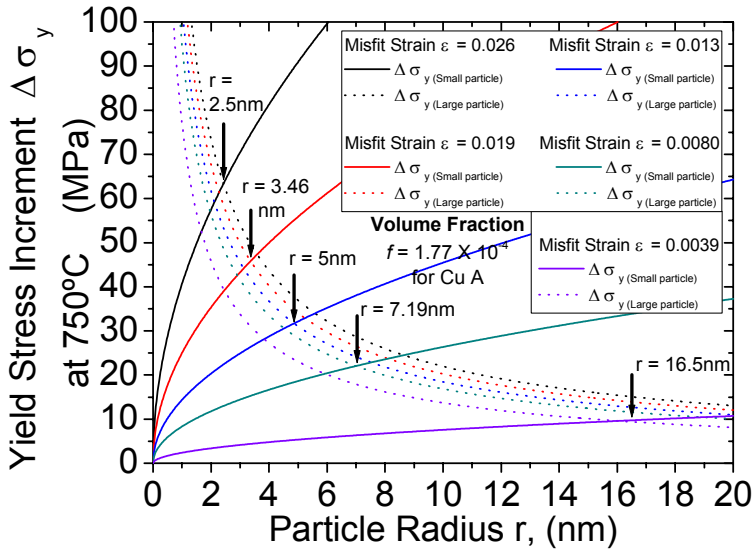

Fig. 4.14. Predicted yield stress increment for semicoherent particles in Cu A.

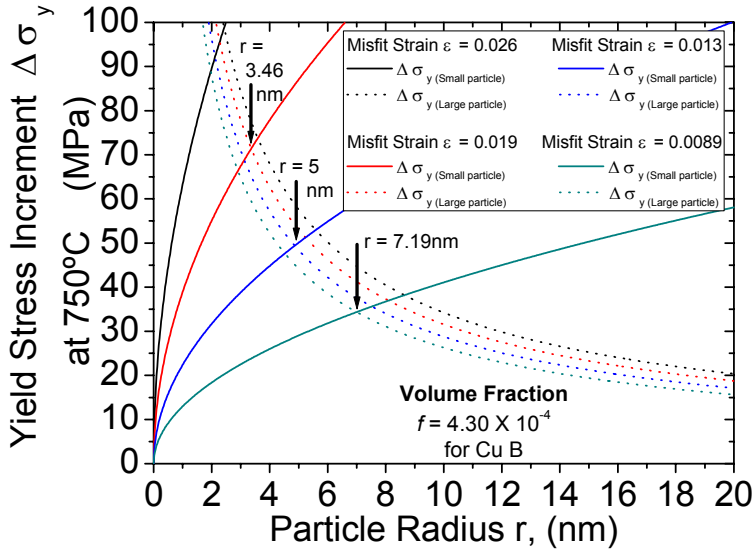

Fig. 4.15. Predicted yield stress increment for semicoherent particles in Cu B.

The semicoherent analysis would seem to work for Cu C if the strengthening was due to particles with 7.1875nm of radius as fig. 4.16 shows. The maximum stress increment predicted on fig. 4.16 is of 42.3MPa for this largest radius found on the TEM samples. And the peak back stress observed is of 38.7MPa while the steady state back stress is 31.1MPa. However by looking at the Cu C TEM images the number of smaller precipitates is evidently greater. The smallest radius accounted (3.438nm) is also shown on fig. 4.16. Despite the near match of the semicoherency equations the presence of smaller particles leads to believe that the Cu_2O precipitates are not behaving semicoherently at 750ºC.

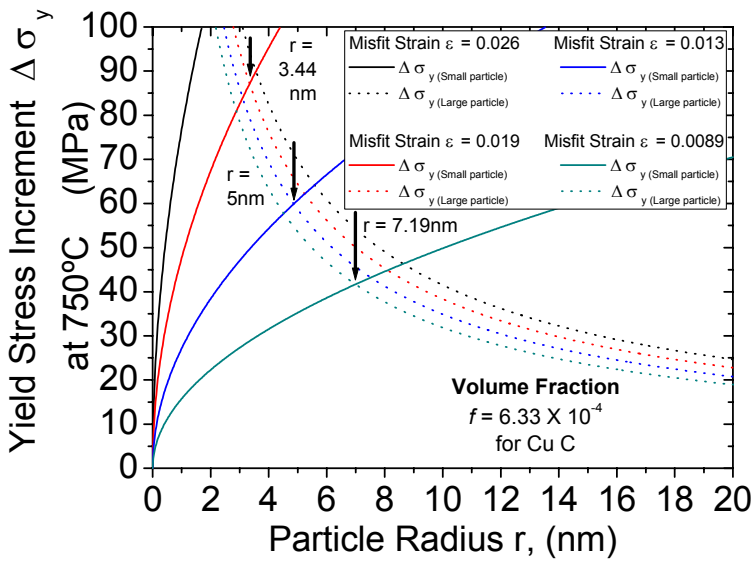

Fig. 4.16. Predicted yield stress increment for semicoherent particles in Cu C.

Gladman [49] has modified the Ashby-Orowan equation for incoherent particles and for this analysis the present author has expressed the shear modulus as a function of temperature, $\mu(T)$. The modified Ashby-Orowan equation provides a better correlation between the size of particles observed on the TEM samples and the predicted increase in stress. The expression is

$$\Delta\sigma_y = \left(0.538\mu b f^{1/2}/X\right)\ln\left(X/2b\right). \qquad (4.13)$$

On eq. 4.13 the particle size X is the real spatial diameter and, like before μ at 750ºC is 29978.55MPa. A plot of the Ashby-Orowan equation at 750ºC is shown on fig. 4.17 employing the particle sizes mentioned before. The visual neatness of the Ashby-Orowan plot allows comparing the three coppers in one figure. The dashed lines were drawn to mark the volume fraction of the three coppers. The dashed lines end at a supposed mean value of particle sizes found. The predicted stress increase on fig. 4.17 for Cu A is low or none. The red dot points to the observed peak back stress (13.6MPa) for Cu B, which should correspond to particles having 25nm diameter. Figure 4.17 predicts a higher stress for the particles found, which were of about 6.9nm. Like for the semicoherent equations Cu B does not seem to approach the higher stresses expected. Although an Ashby-Orowan plot for 700ºC seems a good prediction (see fig. 4.18). Concerning Cu C at 750ºC on fig. 4.17 the black square points to the observed peak back stress (38.7MPa), which is almost equal to the value predicted by the modified Ashby-Orowan equation (39.0MPa). Cu C also shows a good correlation at 700ºC between peak back stress and predicted stress increase, as fig. 4.18 shows. The overestimation of the semicoherency equations and the better correlation of the modified Ashby-Orowan equation demonstrates that for the temperatures examined the Cu_2O precipitates behave as having incoherent interfaces. If the TEM images showed clearly that most precipitates had been cut or looped an easier demonstration would have been possible.

The effect of precipitation hardening during hot flow diminishes as the strain rate is lower because enough time is allowed for the thermal component to restore the pinned dislocations. The latter theoretical analyses using semicoherent and incoherent

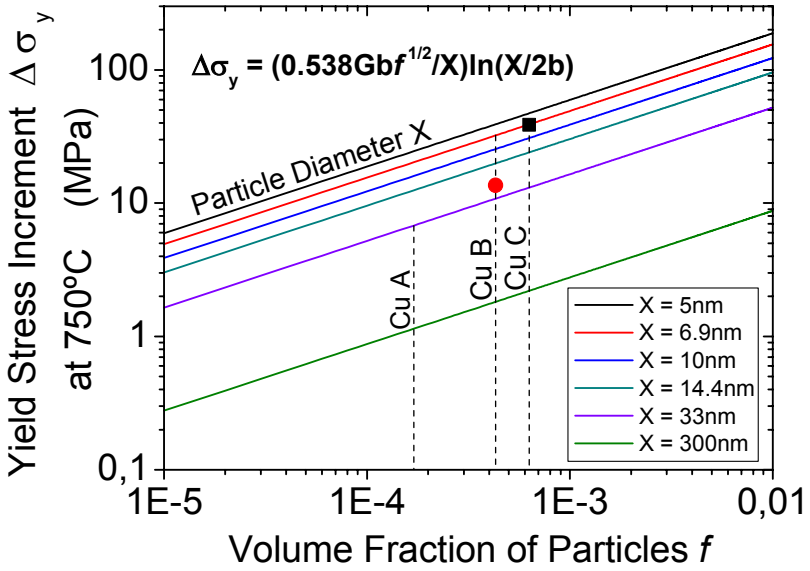

Fig. 4.17. Modified Ashby-Orowan yield stress increment at 750ºC.

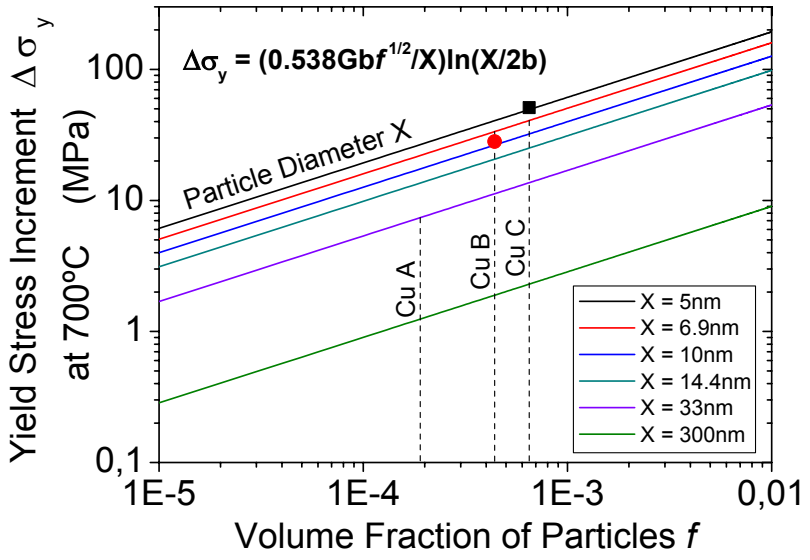

Fig. 4.18. Modified Ashby-Orowan yield stress increment at 700ºC.

relationships that were originally derived neglecting diffusion were only possible because of the assumption that at a high strain rate the diffusion is less capable of helping dislocations by pass precipitates. If $\Delta\sigma_y$ is considered as the saturation back stress produced by the precipitation of particles then a relationship can be suggested to model the back stress when deforming at a particular strain rate, $\dot{\varepsilon}$, and up to a particular deformation ε. The relationship to predict the back stress may have the form of

$$\sigma_O \approx \Delta\sigma_y \left\{ \exp\left[-B_0 \left(\varepsilon/\dot{\varepsilon}\right)^{v_0} \right] \right\} \tag{4.14}$$

where B_0 and v_0 are constants that need to be determined. Relationship 4.14 implicitly acknowledges the role of diffusion rate has in helping dislocations by pass obstacles if

enough time, $\varepsilon/\dot{\varepsilon}$, is allowed. Figure 4.19 shows the behavior of relationship 4.14 where the back stress becomes constant after reaching a high enough strain rate. When B_0 of relationship 4.14 has a lower value than the one shown then that indicates the back stress is less strain rate sensitive at the testing temperature, particularly at higher strain rates. A high value of v_0 increases the slope and would indicate that the back stress is easily affected by the strain rate because dislocations are prone to climb and by pass precipitates at the given test temperature. The relationship proposed would model the back stress as a dependent variable of the mean diameter of the particles, the test temperature, the volume fraction, strain and, the strain rate. Further investigation is needed to assess the reliability of eq. 4.14. However, as an example, for the particular conditions of Cu C at 750ºC and a supposed mean particle diameter of 5nm the constant B_0 is 0.498 and the exponent v_0 is 0.210 for the back stress produced at 0.8 of strain.

Another effect that the Cu_2O precipitates could be producing besides strengthening is grain growth control during hot deformation. The effect of incoherent Cu_2O precipitates on migrating grain borders requires analysis to understand how an increase in oxygen level can influence the dynamically recrystallized grain size. The influence of precipitates on the end microstructure is studied in another chapter.

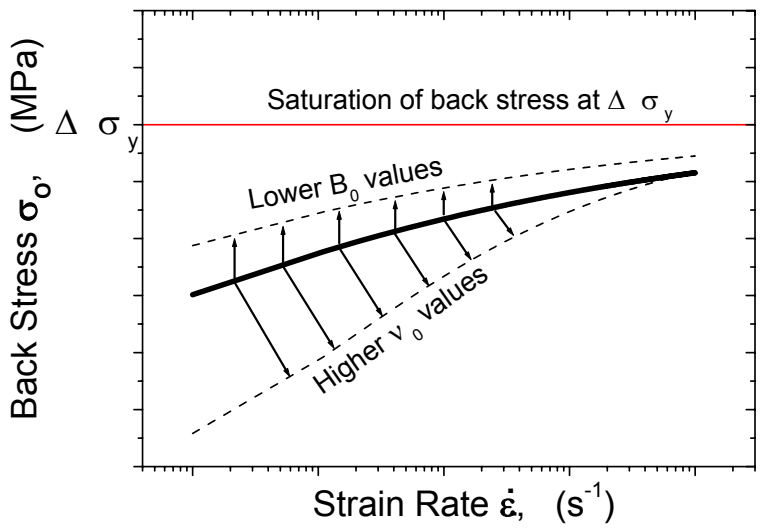

Fig. 4.19. The values of B_0 and v_0 of relationship 4.14 describe the ability of a metal to restore precipitation pinned dislocations during hot flow.

4.6 Conclusions

1) Fire-refined 99.9% pure coppers can present flow stress differences at temperatures below 800ºC caused by precipitation hardening of Cu_2O particles.
2) The Cu_2O precipitates were the only small enough particles found that were capable of reinforcing the metal matrix despite the number of other residual elements. The back stress registered coincided with the presence of Cu_2O precipitates.
3) At the same hot flow conditions the copper with higher oxygen content registered a higher back stress. The coppers tested ranged 26ppm to 62ppm of oxygen.
4) The back stress can be modeled using precipitation-hardening theories adapted for polycrystalline metals and higher temperatures. In general the Cu_2O precipitates behave as having incoherent interfaces with the copper matrix. The modified Ashby-

Orowan relationship [49] can be used as the limiting value where the back stress saturates at a high enough strain rate.

4.7 References

[1] Hondros E.D., McLean D., Cohesion Margin of Copper, Philosophical Magazine vol. 29, (1974) pp. 711-795.

[2] Carlsson Rune, Hot Embrittlement of Copper and Brass Alloys, Scandinavian Journal of Metallurgy, vol. 9, (1980), pp. 25-29.

[3] Archbutt S.L., Prytherch W.E., Effect of Impurities in Copper, British Non-Ferrous Metals Research Association, R. Clay & Sons Limited, Bungay, Suffolk, (1937), pp.1-135.

[4] Saarivirta Matti J., Behavior and Effect of Sulfur on Oxygen-Free High-Purity Copper, Transactions of the ASM, vol. 57, (1964), pp. 133-141.

[5] Esparducer, A., Segarra, M., Espiell F., García, M., Guixà, O., Effects of Pre-Heating Treatment on the Annealing Behavior of Cold-Drawn Fire-Refined Coppers, Journal of Materials Science 36 (2001), pp.241-245.

[6] Tipler H.R., McLean D., Influence of Interface Energy on Creep Rupture, Metal Science Journal, vol. 4, (1970), pp. 103-107.

[7] Smart Jr. J.S., Smith Jr. A.A., Effect of Phosphorus, Arsenic, Sulphur, and Selenium on Some Properties of High-Purity Copper, Trans. AIME, no.166, (1946), pp. 144-155.

*[8] Dies K., Kupfer und Kupferlegierungen in der Technik, 1967.

[9] Aoyama S., Onuki M., Miyake Y., Urao R., Effects of Lead on Annealing Properties of Cold-Drawn Copper Wire, Journal of Materials Science 26, (1991), pp. 3775-3779.

[10] Won Mok Young, Oh Hwan Kyu, Effect of Preheating on the Mechanical Properties of Tough Pitch Copper Made from Copper Scraps, Journal of Material Science, Vol. 32, (1997), pp. 2045-2054.

[11] Edelson B.I., Baldwin JR. W.R., The Effect of Second Phases on the Mechanical Properties of Alloys, Transactions of the ASM, vol.55 (1962), pp. 230-250.

[12] Camurri C.P., López M.J., Leon P.C., Rheology and Metal Forming of Fire-Refined Copper, Materials Characterization 47 (2001), pp. 253-257.

[13] Camurri C., López M., Sánchez M., Soto J., Impurities in Fire Refined Copper. Effect of Oxygen on Ductility, EDP Congress 1994, The Minerals, Metals & Materials Society (1993), pp.601-613.

[14] Camurri C., López M., Soto J., Influence de la teneur en oxygène sur la ductilité du cuivre raffiné au feu entre la temperature ambiante et 800ºC, La Revue de la Métallurgie-CIT/Science et Génie des Matériaux, Decembre (1994), pp. 1797-1803.

[15] Nieh T.G., Nix W.D., Embrittlement of Copper Due to Segregation of Oxygen to Grain Boundaries, Metallurgical Transactions A, vol. 12A, may (1981), pp. 893-901.

[16] Ravichandran, N., Prasad, Y. V. R. K., Influence of Oxygen in Dynamic Recrystallization During Hot Working of Polycrystalline Copper, Materials Science and Engineering, A156 (1992) pp. 195-204.

[17] Hull Derek, Fractography: observing, measuring, and interpreting fracture surface topography, Cambridge University Press, Cambridge, (1999), pp. 235-238.

[18] Hull D., Rimmer D.E., The Growth of Grain Boundary Voids Under Stress, Philosophical Magazine, vol. 4 (1959), pp. 673-687.

[19] Bleakney H. H., The Ductility of Metals in Creep-Rupture Tests, Canadian Journal of Technology, vol. 30, (1952), pp. 340-351.

[20] Fujiwara, S., Abiko, K., Ductility of Ultra high Purity Copper, Journal de Physique IV, Colloque C7, supplément au Journal de Physique III, vol. 5, November 1995.

[21] Gao, W., Belyakov, A., Miura, H., Sakai, T., Dynamic Recrystallization of Copper Polycrystals with different impurities, Materials Science and Engineering A265 (1999) pp. 233-239.

[22] García V.G., Cabrera J.M., Prado J.M., Dynamically Recrystallized Grain Size of Some Commercial Purity Coppers, Proceedings of the First Joint International Conference on Recrystallization and Grain Growth (Aachen), Eds. Gottstein G. And Molodov D.A., Springer-Verlag, Berlin, (2001), pp.515-520.

[23] Sellars C.M., Tegart W.J.McG., La Relation entre la Résistance et la Structure dans la Déformation à Chaud, Memoires Scientific Rev. Métallurg. LXIII, no. 9, (1966), pp.731-746.

[24] Wong W.A., Jonas J.J., Aluminum Extrusion as a Thermally Activated Process, Transactions of the Metallurgical Society of AIME, vol. 242, November 1968, pp. 2271-2280.

[25] Jonas J.J., Sellars C.M., Tegart W.J.McG., Strength and Structure Under Hot-Working Conditions, Metallurgical Reviews, Vol. 14, No. 1, (1969), pp. 1-24.

[26] Tanaka K., Nakamura T., Hoshida Y., Hara S., Determination of the Constants in the Zener-Hollomon Hyperbolic Equation for High Temperature Deformation, Res Mechanica 12 (1984) 41-57.

[27] Garofalo F., An Empirical Relationship Defining the Stress Dependence of Minimum Creep Rate in Metals, Transactions of the Metallurgical Society of AIME, Vol. 227, April (1963), pp. 351-355.

[28] Frost H.J., Ashby M.F., Deformation-Mechanism Maps, The Plasticity and Creep of Metals and Ceramics, Pergamon Press, Oxford, (1982), pp. 1-165.

[29] Weertman Johannes, Dislocations Climb Theory of Steady-State Creep, Transactions of the ASM, Vol. 61, (1968) pp. 681-694.

[30] Seeger Alfred, The Generation of Lattice Defects by Moving Dislocations, and its Application to the Temperature Dependence of the Flow-Stress of F.C.C. Crystals, Philosophical Magazine, vol. 16, no. 282, November (1955), pp. 1194-1217.

[31] Cabrera J.M., Prado J.M., Simulación de la Fluencia en Caliente de un Acero Microaleado con un Contenido Medio de Carbono I parte. Aproximación Teórica, Rev. Metal Madrid, 33 (2), 1997, pp. 80-88.

[32] Cabrera J.M., Prado J.M., Simulación de la Fluencia en Caliente de un Acero Microaleado con un Contenido Medio de Carbono II parte. Recristalización Dinámica: Inicio y Cinética, Rev. Metal Madrid, 33 (3), 1997, pp. 143-152

[33] Cabrera J.M., Prado J.M., Simulación de la Fluencia en Caliente de un Acero Microaleado con un Contenido Medio de Carbono III parte.Ecuaciones Constitutivas, Rev. Metal Madrid, 33 (4), 1997, pp. 215-228.

[34] Cabrera J.M., Jonas J.J., Prado J.M., Flow Behaviour of Medium Carbon Microalloyed Steel Under Hot Working Conditions, Materials Science and Technology, vol. 12, July (1996), pp. 579-585.

[35] Cabrera J.M., Al Omar A., Jonas J.J., Prado J.M., Modeling the Flow Behavior of a Medium Carbon Microalloyed Steel Under Hot Working Conditions, Metallurgical and Materials Transactions A, vol. 28A, November (1997), pp. 2233-2244.

[36] Samanta Shyam Kinkar, On Relating the Flow Stress of Aluminium and Copper to Strain, Strain Rate and Temperature, Int. J. Mech. Sci., Pergamon Press, vol. 11, (1969), pp. 433-453.

[37] Samanta S.K., Dynamic Deformation of Aluminium and Copper at Elevated Temperatures, J. Mech. Phys. Solids, vol. 19, no. 1, February (1971), pp. 117-135.

[38] Blaz L. Korbel A., Effect of Hot Deformation on Grain Size in Deformed and Annealed Copper, Hot Working and Forming Processes, ed. C.M. Sellars and G.J. Davies, The Metals Society, London, (1980), pp.57-61.

[39] Sherby, O. D., Factors Affecting the High Temperature Strength of Polycrystalline Solids, Acta Metallurgica, vol. 10, February,(1962), pp. 135-147.

[40] García V.G., Cabrera J.M., Riera L.M., Prado J.M., Hot Deformation of a Commercial Purity Copper, Proceedings of Euromat 2000: Advances in Mechanical Behaviour, Plasticity and Damage, vol. 2, Elsevier Science, Oxford, pp.1357-1362.

[41] Johnson Robert E., Rhines F.N., Cu-O (Copper-Oxygen), Phase Diagrams of Binary Alloy Systems, Metals Handbook, ASM, pg. 295, pg. 357.

[42] Lide, David R., CRC Handbook of Chemistry and Physics, 72nd Edition, CRC Press, Boca Raton, 1991.

[43] Orowan E., Problems of Plastic Gliding, Proceedings of the Physical Society of London, Vol. 52, No. 8, (1940), pp. 8-22.

[44] Kocks U.F., Argon A.S., Ashby M.F., Progress in Material Science Vol. 19: Thermodynamics and Kinetics of Slip, Editors: Chalmers B., Christian J.W., Massalski T.B., Pergamon Press Ltd., Headington Hill Hall, Oxford, England, (1975), pp. i-291.

[45] Evans A.G., Rawlings R.D., The Thermally Activated Deformation of Crystalline Materials, Phys. Stat. Sol., Vol. 34, No. 9, (1969), pp. 9-31.

[46] De Meester B., Yin C., Doner M., Conrad H., Thermally Activated Deformation of Crystalline Solids, Rate Processes in Plastic Deformation of Materials ASM, (1975), pp. 175-226.

[47] Follansbee P.S., Kocks U.F., A Constitutive Description of the Deformation of Copper Based on the Use of the Mechanical Threshold Stress as an Internal State Variable, Acta Metall. Vol. 36, No. 1, (1988), pp. 81-93.

*[48] Orowan E., Internal Stress in Metals and Alloys, The Institute of Metals, London, (1948), 451.

[49] Gladman T., Precipitation hardening in metals, Materials Science and Technology, vol. 15, jan (1999), pp.30-36.

[50] Kocks U.F., The Relation Between Polycrystal Deformation and Single-Crystal Deformation, Metallurgical Transactions, Vol. 1, May (1970), pp. 1121-1143.

[51] Taylor G.I., Plastic Strain in Metals, Journal of the Institute of Metals, May Lecture (1938), pp. 307-324.

[52] Groves G.W., Kelly A., Independent Slip Systems in Crystals, Philosophical Magazine, Vol. 8, (1963), pp. 877-887.

[53] Nemat-Nasser Sia, Li Yulong, Flow Stress of F.C.C. Polycrystals with Application to OFHC Cu, Acta mater. Vol. 46, No. 2, (1998), pp. 565-577.

[54] Porter D.A., Easterling K.E., Phase Transformations in Metals and Alloys, 2nd Ed., Chapman & Hall, London, (1981), pp. 138-163.